

A new method for determining the sensitivity of X-ray imaging observations and the X-ray number counts

A. Georgakakis*, K. Nandra, E. S. Laird, J. Aird, M. Trichas

Astrophysics Group, Blackett Laboratory, Imperial College, Prince Consort Rd, London SW7 2AZ, UK

30 October 2018

ABSTRACT

We present a new method for determining the sensitivity of X-ray imaging observations, which correctly accounts for the observational biases that affect the probability of detecting a source of a given X-ray flux, without the need to perform a large number of time consuming simulations. We use this new technique to estimate the X-ray source counts in different spectral bands (0.5–2, 0.5–10, 2–10 and 5–10 keV) by combining deep pencil-beam and shallow wide-area *Chandra* observations. The sample has a total of 6295 unique sources over an area of 11.8deg² and is the largest used to date to determine the X-ray number counts. We determine, for the first time, the break flux in the 5–10 keV band, in the case of a double power-law source count distribution. We also find an upturn in the 0.5–2 keV counts at fluxes below about 6×10^{-17} erg s⁻¹ cm⁻². We show that this can be explained by the emergence of normal star-forming galaxies which dominate the X-ray population at faint fluxes. The fraction of the diffuse X-ray background resolved into point sources at different spectral bands is also estimated. It is argued that a single population of Compton thick AGN cannot be responsible for the entire unresolved X-ray background in the energy range 2–10 keV.

Key words: methods: data analysis – methods: miscellaneous – methods: statistical – surveys – X-rays: galaxies – X-rays: diffuse background

1 INTRODUCTION

X-ray observations have complex instrumental effects that have a strong impact on the detection probability of point sources. The size and the shape of the Point Spread Function (PSF) for example vary across the detector. Also, the mirrors of X-ray telescopes are more efficient at collecting photons from sources close to the centre of the field of view (vignetting). This loss of sensitivity effectively translates to a reduction of the exposure time with increasing off-axis angle. In addition to the instrumental effects above, the application of any source detection software on an X-ray image also introduces biases (e.g. Kenter & Murray 2003; Wang 2004). Brighter sources have a higher probability of detection compared to fainter ones. Background fluctuations result in spurious detections that are inevitably present, hopefully in small numbers, in any X-ray catalogue. Statistical variations of the source counts combined with the steep $\log N - \log S$ of the X-ray population result in brighter measured fluxes for the detected sources compared to their intrinsic ones (Eddington bias). This effect becomes more severe close to the detection threshold of a given X-ray observation.

For a wide range of applications it is important to quantify these effects accurately in order to understand the type of sources

a given X-ray observation is (or is not) sensitive to. For example, the large scale structure of X-ray sources is often estimated using the angular or the spatial correlation functions (e.g. Basilakos et al. 2004, 2005; Gilli et al. 2005; Miyaji et al. 2007). For this exercise one needs to construct a simulated comparison sample of sources with random spatial distribution across the surveyed area. These mock catalogues should follow the same instrumental and source detection related biases as the real sample. If not any recovered signal will be heavily contaminated. Also, for the estimation of the luminosity function of X-ray selected populations one needs to determine the volume of the survey which is accessible to a source with a particular flux and spectral shape (e.g. Hasinger et al. 2005; Nandra et al. 2005a; Aird et al. 2008). Understanding the sensitivity of a given X-ray observation to AGN of variable obscuration and luminosity is of key importance for studies of the diffuse X-ray background (e.g. La Franca 2005; Akylas et al. 2006; Gilli, Comastri & Hasinger 2007). Finally, in order to constrain the number density of X-ray sources to the faintest fluxes accessible to a given observation it is essential to have an accurate estimate of the total surveyed area over which a source of a given flux can be detected (e.g. Kim et al. 2007a).

The point source selection function of a given X-ray observation can be represented in the form of a sensitivity map, which should provide an estimate of the probability that a source with

* Marie Curie fellow

a flux f_X in a certain energy band will be detected across the detector. One approach to construct such a map is to perform a large number of ray tracing simulations (e.g. Cappelluti et al. 2007; Kim et al. 2007a). Artificial sources with a wide range of fluxes are placed at different pixels on the detector assuming a realistic model for the (instrumental and cosmic) background. The fraction of sources picked up by the detection method as a function of detector position and flux provides an estimate of the sensitivity of the particular observation. This approach however, is time consuming and difficult to apply to large numbers of observations with different setups. These simulations also cannot fully correct for the Eddington bias, at least not for individual sources. This problem has been addressed recently by Kenter & Murray (2003) who presented a novel method for the construction of X-ray number counts that accounts for both the Eddington bias of individual detections as well as the variable point source detection threshold across the survey area. Wang (2004) further developed this technique to avoid the need for cumbersome ray tracing simulations.

In this paper we extend these previous studies by presenting an improved method for constructing point source sensitivity maps for X-ray imaging observations. The backbone of our approach is the point source detection method presented by Nandra et al. (2005b). Combined together these two techniques provide a simple and efficient way of detecting sources and determining accurately their selection function self consistently by taking into account both instrument specific effects and the source detection biases. As a demonstration of our method we present the X-ray number counts in different energy bands, 0.5–2, 0.5–10, 2–10 and 5–10 keV. Future applications include the determination of the angular correlation function of X-ray sources and the estimation of the luminosity function of AGN. Finally, our method is build around *Chandra* data but can be easily extended to *XMM-Newton*.

2 SOURCE DETECTION

The point source detection method has a central role in the construction of sensitivity maps. The adopted approach is fully described by Nandra et al. (2005b) and has recently been extended to use a new set of PSFs generated by MARX (Model of AXAF Response to X-rays) as discussed in Laird et al. (2008 in prep.). Elliptical apertures are used to estimate the Encircled Energy Fraction (EEF) as a function of semi-major axis radius. However, for the source detection and sensitivity map construction we use circular apertures with areas equal to that of the 70 per cent EEF ellipses. The uncertainty introduced by this approximation is < 2 per cent. The source extraction is based on pre-selection of positive fluctuations using the WAVDETECT task of CIAO at a low probability threshold of 10^{-4} . The total counts (source and background) at the position of each candidate source are then extracted using a circular area equal to the 70 per cent EEF elliptical aperture. The mean expected background within the detection cell is determined by scaling the counts from a local annulus centred on the source with inner aperture equal to 1.5 times the 90 per cent EEF radius and width of 50 arcsec. The probability that the candidate source is a random fluctuation of the background is estimated assuming Poisson statistics. A threshold of $< 4 \times 10^{-6}$ is adopted for a source candidate to be considered a detection. At this level about 0.5 false sources per *Chandra* image are expected (Laird et al. 2008 in prep.). This method is simple and efficient resulting in higher sensitivity and fewer spurious detections compared to alternative wavelet-based only techniques. However, the most important fea-

ture of the method is that the detection cell has a fixed size at each position on the detectors, making the construction of the sensitivity maps straightforward.

3 SIMULATIONS

We use MARX to simulate *Chandra* observations and to validate the method for constructing sensitivity maps. MARX is a suite of programs that perform detailed ray tracing simulations to determine how *Chandra* responds to astrophysical sources. In this study we simulate point sources in the 2–10 keV spectral band with a built-in distribution per unit X-ray flux interval, dN/df_X , that follows a double power-law of the form

$$\frac{dN}{df_X} = \begin{cases} K \left(\frac{f_X}{f_{ref}} \right)^{\beta_1}, & f_X < f_b, \\ K' \left(\frac{f_X}{f_{ref}} \right)^{\beta_2}, & f_X \geq f_b, \end{cases} \quad (1)$$

where the normalisation constants K and K' follow the relation $K' = K (f_b/f_{ref})^{\beta_1 - \beta_2}$, f_b is the X-ray flux of the break of the double power-law, $f_{ref} = 10^{-14} \text{ erg s}^{-1} \text{ cm}^{-2}$ is the normalisation flux and β_1, β_2 are the power-law indices for fluxes fainter and brighter than the break flux respectively. The cumulative counts follow the relations

$$N(> f_X) = \begin{cases} K \frac{f_{ref}}{1+\beta_1} \left(\left(\frac{f_b}{f_{ref}} \right)^{1+\beta_1} - \left(\frac{f_X}{f_{ref}} \right)^{1+\beta_1} \right) + \\ K' \frac{f_{ref}}{1+\beta_2} \left(\frac{f_b}{f_{ref}} \right)^{1+\beta_2}, & f_X < f_b, \\ K' \frac{f_{ref}}{1+\beta_2} \left(\frac{f_X}{f_{ref}} \right)^{1+\beta_2}, & f_X \geq f_b, \end{cases} \quad (2)$$

For the simulations we adopt the best-fit parameters determined by Kim et al. (2007a) for the 2–8 keV counts: $\beta_1 = -1.58$, $\beta_2 = -2.59$ and $f_b(2 - 10 \text{ keV}) = 2 \times 10^{-14} \text{ erg s}^{-1} \text{ cm}^{-2}$. The break flux determined by Kim et al. (2007a) in the 2–8 keV band is shifted to the 2–10 keV energy range assuming $\Gamma = 1.4$. The normalisation is fixed so that there are 7000 sources per square degree brighter than $f_X(2 - 10 \text{ keV}) = 10^{-16} \text{ erg s}^{-1} \text{ cm}^{-2}$, i.e. similar to the observed density of X-ray sources.

We adopt an X-ray spectrum with $\Gamma = 1.4$ and a total exposure time of 200 ks. Simulated ACIS-I event files are constructed by randomly placing within the *Chandra* field of view point sources with fluxes in the range $f_X(2 - 10 \text{ keV}) = 5 \times 10^{-17} - 10^{-12} \text{ erg s}^{-1} \text{ cm}^{-2}$. MARX does not simulate the *Chandra* background. This is added to the simulated images using the quiescent background event files produced by the ACIS calibration team using blank sky observations. In the next sections it is demonstrated that using the proposed method for quantifying the sensitivity of X-ray imaging observations we can successfully recover the input source count distribution.

4 SENSITIVITY MAP CONSTRUCTION

The sensitivity map is an estimate of the probability that a source with flux f_X in a certain energy band will be detected across the detector. This probability depends on the detector characteristics, the adopted observational strategy and the specifics of the source detection. Instead of extensive simulations one can use statistics to approximate the source detection process, as this is essentially a Poisson experiment. Any source extraction method estimates the

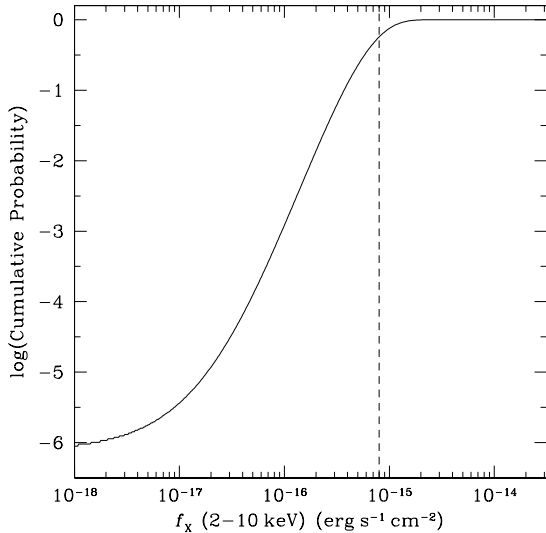


Figure 1. Probability that a source with hard flux $f_X(2-10\text{ keV})$ and a power-law spectrum with $\Gamma = 1.4$ is detected within an element where the mean local background is $B = 0.14$ and the detection threshold is $L = 5$, typical of the aimpoint region of a 200 ks *Chandra* observations. The vertical dashed line shows the approximate limiting flux of such an observation (e.g. Nandra et al. 2005b). Fluctuations of the total counts (source and background) within the cell have a finite probability of producing a detection even if the real source has flux well below the formal survey limit.

Poisson probability that the observed counts in a detection cell arise from random fluctuations of the background. The important parameters in this exercise are the size and shape of the detection cell, which is well defined in our source detection method, and the Poisson probability threshold, P_{thresh} , below which an excess of counts is considered a source. By fixing P_{thresh} one sets the minimum number of photons in a cell, L , for a formal detection.

The observed counts in a detection cell have a background and possibly a source component. Either of them can fluctuate so that their sum is higher than L . This either produces a spurious source in the case of a background fluctuation or can make a faint source appear with a brighter observed flux, i.e. the Eddington bias. Both these effects are part of the source selection process and should be accounted for by the sensitivity map.

The first step to construct such an image is to estimate the source-free background across the detector. This has an instrumental and a cosmic component, with the latter coming from sources below the sensitivity of the observation or photons in the extended wings of the PSF of detected sources. The background map is estimated using custom routines to first remove the counts in the vicinity of detected sources using an aperture size that is 1.5 times larger the 90 per cent EEF radius. Pixel values in the source regions are replaced by sampling from the distribution of pixel values in local background regions. These are defined by annuli centred on each source with inner apertures equal to 1.5 times the 90 per cent EEF radius and widths of 50 arcsec. The resulting maps can then be used to estimate the mean expected background counts within any detection cell, B . The cumulative probability that the observed counts in a particular detection cell will exceed L is

$$P_B(\geq L) = \gamma(L, B), \quad (3)$$

where the function $\gamma(a, x)$ is defined

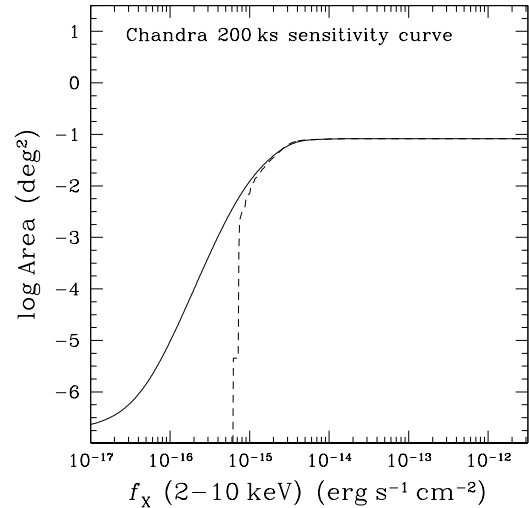


Figure 2. Sensitivity curve in the 2-10 keV spectral band of a simulated 200 ks *Chandra* observations estimated using the method described in this paper (continuous curve). The dashed line is the area curve that does not account for the Poisson probability density distribution of the total observed counts in the detection cell.

$$\gamma(a, x) = \frac{1}{\Gamma(a)} \int_0^x e^{-t} t^{a-1} dt. \quad (4)$$

Adopting a detection threshold P_{thresh} one can invert equation 3 numerically to estimate the (integer) detection limit L for a cell with mean expected background B . Repeating this exercise for different cells across the image one can determine L as a function of position (x, y) on the detector. This 2-D image of L values is the sensitivity map. Note that the sensitivity map is independent of the spectral shape of the source. A useful 1-D representation of this image, with a wide range of applications, is the total detector area in which a source with flux f_X can be detected. The cumulative distribution of the area plotted as function of f_X is often referred to as a sensitivity curve. This is constructed as follows. For a source with flux f_X and a given spectral shape ($\Gamma = 1.4$ in this paper) we can determine the probability of detection in a cell with mean background B and detection limit L . The total observed counts in the cell are $T = B + S$, where S is the mean expected source contribution. In practise this depends on the observation exposure time, the vignetting of the field at the position of the cell, embodied in the exposure map, and the fraction of the total source counts in the cell because of the PSF size.

$$S = f_X \times t_{exp} \times C \times \eta. \quad (5)$$

Where t_{exp} is the exposure time at a particular position after accounting for instrumental effects, C is the conversion factor from flux to count rate for the adopted source spectral shape and η is the encircled energy fraction at the particular position. Both B and S fluctuate and therefore using equation 3 the probability their sum exceeds the detection threshold is $P_{T, f_X}(\geq L) = \gamma(L, T)$. Figure 1 plots $P_{T, f_X}(\geq L)$ against f_X for a particular choice of B and L values, typical of a detection cell close to the aimpoint of a 200 ks *Chandra* observation in the 2-10 keV energy band. At faint fluxes, $S \rightarrow 0$ and $P_{T, f_X}(\geq L) \rightarrow P_{thresh}$, because this is the finite probability of a random background fluctuation above the limit L , i.e. spurious detections.

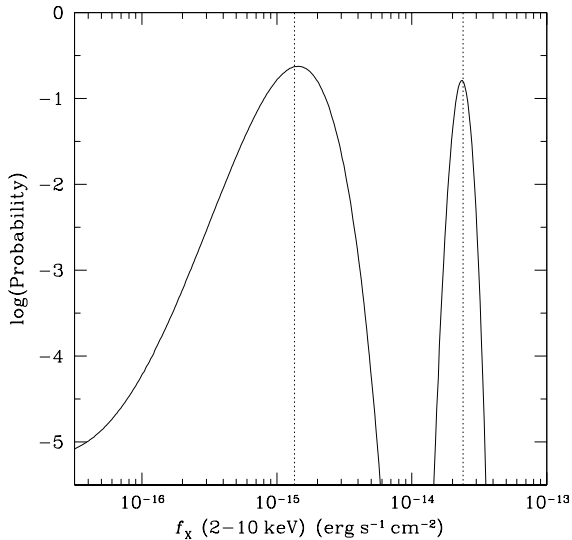


Figure 3. Flux probability density distribution estimated from equation 6 for sources detected in the 200 ks *Chandra* ACIS-I simulation. The curves estimate the probability of observing exactly N counts (source and background) from a source with flux f_X . The normalisation is arbitrary. Examples of two simulated sources are shown. The faint one has a total number of counts within the 70 per cent EEF cell of $T = 9$ and a mean local background of $B = 0.41$ counts. For the bright source $T = 120$ and $B = 3.06$ counts. The dotted vertical lines mark the input fluxes of the two sources in the simulated field, $f_X(2-10) = 1.35 \times 10^{-15}$ and $2.40 \times 10^{-14} \text{ erg s}^{-1} \text{ cm}^{-2}$ respectively. The contribution of each source to the number counts is estimated by dividing the probability distribution curves with the sensitivity curve of Fig. 2.

The sensitivity curve is the sum of the $P_{T, f_X}(\geq L)$ distributions of individual detection cells. This is graphically shown in Figure 2 for the 2-10 keV band of a simulated 200 ks *Chandra* pointing. For comparison we also show the sensitivity curve of this field calculated adopting the standard approach of assigning a single limiting flux to a detection cell. This is estimated by assuming that the minimum net counts for a source to be detected in the cell are $S = L - B$. This method ignores the fact that the total observed photons in a cell, source and background, fluctuate according to the Poisson distribution. These fluctuations become increasingly important toward the low count limit, i.e. faint fluxes and/or low background. The method presented here correctly accounts for this effect. Also, the finite number of spurious detections that are inevitably present in any source catalogue is factored into the sensitivity curve estimation.

5 X-RAY NUMBER COUNT ESTIMATION

In this section we describe the methodology for determining the surface density of X-ray sources on the sky as a function of flux using the new approach for constructing sensitivity maps. The standard method of estimating number counts, cumulative $N(> f_X)$ or differential dN/df_X , is to weigh each source of flux f_X with the inverse of the solid angle in which it can be detected. The drawback of this approach is that it assigns a single flux to a source and therefore does not account for the fact that the observed total counts in the detection cell can be produced by sources with a range of f_X according to a probability distribution that can be estimated using

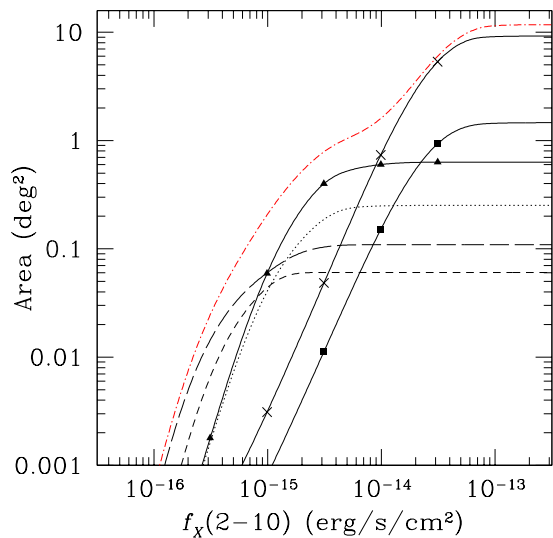


Figure 4. Sensitivity curve in the hard band (2-10 keV) for the different *Chandra* surveys used to determine the differential X-ray source counts. XBOOTES: continuous line with the crosses; ELAIS-N1: continuous line marked with squares; EGS: The continuous line marked with triangles; ECDF-S: dotted line; CDF-S: short-dashed line; CDF-N: longed-dashed line. The (red) dashed-dotted line is the sum of the individual curves. The different slopes between the shallow and the deep surveys is the result of the outer regions becoming background limited.

Poisson statistics. If the mean expected total counts in the detection cell are $T = S + B$, where S is determined as a function of flux from equation 5 and B is the local background value then the probability of finding the observed number of total counts N (source and background) is

$$P(f_X, N) = \frac{T^N e^{-T}}{N!} f_X^\beta. \quad (6)$$

where the last term, f_X^β , is for the Eddington bias and assumes that the differential X-ray source counts follow a power-law of the form $dN/df_X \propto f_X^\beta$. Equation 6 is graphically shown in Figure 3 in the case of a particular source drawn from the simulations described in section 3. The X-ray number counts are determined by simply dividing the sum of the probability distributions of individual sources, $P(f_X, N)$, with the sensitivity curve determined in the previous section. This approach has the advantage that it accounts for source and background fluctuations, the Eddington bias and spurious detections in the catalogue.

Determination of $P(f_X, N)$ for individual sources requires however, knowledge of the source count power-law index β . This is estimated by applying maximum likelihood (ML) methods to the unbinned data. The probability of the source i with total number of counts N_i in the surveyed area is

$$P_i = \frac{\int P(f_X, N_i) df_X}{\int dN/df_X A(f_X) df_X}. \quad (7)$$

The likelihood of a particular set of data is estimated by multiplying the probabilities P_i of individual sources. We can then estimate the power-law index β that maximises the likelihood. It is straightforward to generalise the form for P_i in the case of a source count distribution that follows the double power-law of equation 1.

Table 1. Stacking results

Survey	Obs. IDs	Exposure (ks)	Area (deg ²)	Sources
(1)	(2)	(3)	(4)	(5)
CDF-N	580, 957, 966, 967, 1671, 2232, 2233, 2234, 2344, 2386, 2421, 2423, 3293, 3294, 3388-3391, 3408, 3409	2000	0.11	516
CDF-S	581 441 582 1672 2405 2239 2312 2313 2406 2409 1431	900	0.06	270
ECDFS	5015-5022, 6164	250	0.25	592
EGS	3305, 4357, 4365, 5841-5854, 6210-6223, 6366, 6391, 7169 7180, 7181, 7187, 7188, 7236, 7237, 7238, 7239	200	0.63	1325
EN1	5855-5884	5	1.47	545
XBOOTES	3596-3660, 4218-4272, 4277-4282	5	9.24	3056

The columns are: (1): Survey name; (2): *Chandra* observation IDs used for each survey; (3) exposure time in ks. In the case of multiple pointings this is the mean exposure time; (4) total surveyed area in deg². For the ECDFS this includes the overlap with the CDF-S; (5) total number of sources in each survey. The ECDFS sources include those overlapping with the CDF-S.

We demonstrate this technique using the simulations described in section 3. The source detection code described in section 2 and the sensitivity map construction method of the previous section are applied to a total of 10 mock *Chandra* fields. We recover the input source count distribution in the 2-10 keV band by combining the 10 individual simulated source lists. Using the ML method we estimate the bright and faint-end power-law indices as well as the break flux, $\beta_1 = -1.62_{-0.06}^{+0.08}$, $\beta_2 = -2.73_{-0.37}^{+0.30}$ and $f_b = (2.0 \pm 0.6) \times 10^{-14} \text{ erg s}^{-1} \text{ cm}^{-2}$, in good agreement with the input values listed in section 3.

6 APPLICATION TO REAL DATA

We apply the methods developed in the previous sections to real *Chandra* data to determine the differential source counts in the 4 standard X-ray spectral bands, soft (0.5-2 keV), hard (2-10 keV), ultra-hard (5-10 keV) and total (0.5-10 keV). We combine observations from 6 *Chandra* surveys, both deep pencil-beam and shallow wide-area. Table 1 presents information on these surveys, which include the *Chandra* Deep Field North and South (CDF-N/S), the Extended *Chandra* Deep Field South (ECDFS), the Extended Groth Strip (EGS), the ELAIS-N1 (EN1) and the XBOOTES survey. The combined sample has a total of 6295 unique sources, detected in different spectral bands, over a total area of 11.8 deg². This is the largest sample to date used for the determination of the X-ray number counts and can only be compared with the recent work of Kim et al. (2007a) who combined observations from the CHAMP survey (Kim et al. 2007b) with the *Chandra* Deep Fields.

The data from these surveys were reduced and analysed in the same way following methods described by Nandra et al. (2005b) and Laird et al. (2008 in prep.). Briefly, standard reduction steps are followed using the CIAO version 3.2 data analysis software. Observations corresponding to the same pointing are merged into a single event file. The ECDFS, EGS, EN1 and XBOOTES surveys include multiple pointings, 4, 8, 30 and 126 respectively. The CDF-S and the ECDFS observations although largely overlapping are treated as separate surveys. This is to avoid problems arising from merging regions with significantly different PSFs. Images are constructed in four energy bands 0.5-7.0 keV, 0.5-2.0 keV, 2.0-7.0 keV and 4.0-7.0 keV. The X-ray catalogue for each spectral band is constructed using the source detection method of section 2 adopting a Poisson detection probability threshold of 4×10^{-6} . The total number of

unique sources in each survey is shown in Table 1. In the case of duplicate sources in the overlap regions of adjacent pointings in the EGS, ECDFS and EN1 surveys we keep the detection with the smallest off-axis angle. Also for the ECDFS we exclude sources that overlap with the deeper CDF-S survey. The count rates in the 0.5-7.0, 0.5-2.0, 2.0-7.0 and 4.0-7.0 keV bands are converted to fluxes in the standard total, soft, hard and ultra-hard bands assuming a power-law X-ray spectrum with index $\Gamma = 1.4$ and Galactic absorption appropriate for each field. We note that this assumption ignores the hardening of the X-ray spectra with decreasing flux (e.g. Mainieri et al. 2002) or the different spectral properties of different X-ray source populations (e.g. AGN vs normal galaxies).

We apply the methods of section 4 to estimate the sensitivity curves of the surveys listed in Table 1 taking into account overlapping regions (e.g. ECDFS and CDF-S). These are presented in Figure 4 for the hard spectral band, 2-10 keV. We follow the prescription of section 5 to construct and to fit the differential counts using the double power-law equation 1. The maximum likelihood parameters for the 4 standard spectral bands are listed in Table 2. The results for the differential (normalised to the Euclidean slope) and cumulative number counts are plotted in Figures 5 and 6. The errorbars in these figures are estimated using 100 bootstrap resamples of the data. We note that systematic uncertainties associated with the use of a fixed Γ for the flux estimation or the EEFC corrections are not taken into account in the calculation of errors. With decreasing flux the area of the survey sensitive to sources of that flux becomes smaller. As a result below a certain limit the observation does not provide a reliable census of the X-ray source population. We choose to plot the number counts to the flux limit corresponding to 1 per cent of the total surveyed area. This cutoff applies only to the graphical representation of the number counts and does not affect the ML calculation, where the decreasing survey area with decreasing flux is fully accounted for in the calculation. The adopted cutoff is typically 1.5-2 times fainter than the standard flux limit of a particular observation (see Figure 2). As a result the number counts derived here extend to fluxes that are 1.5-2 times fainter than previous determinations. This is demonstrated in Figure 5 for the 0.5-2 and 2-10 keV bands, for which accurate estimates of the differential counts are available in the literature. Our work also has the advantage that all the fields used to determine the number counts have been analysed in a homogeneous way and that *all* the detected sources, even those close to the flux limit of the surveys in Table 1, have been used in the calculation. This is because our approach for determining the $\log N - \log S$ correctly accounts for the completeness and flux bias corrections, particularly for sources with few photons close to the detection limit of a given survey.

The best-fit parameters for the 0.5-2, 2-10 and 0.5-10 keV bands in Table 1 are in good agreement with recent estimates by Kim et al. (2007a), who also combined deep pencil-beam surveys with shallow observations over a wide area with *Chandra* to determine the number counts in the 0.5-2, 2-8 and 0.5-8 keV bands. Also presented here for the first time, is the $\log N - \log S$ in the 5-10 keV band over 4 dex in flux. This wide flux range allows the determination of the flux of the break in the double power-law representation of the 5-10 keV number counts.

In Figure 5 the soft band source counts at fluxes fainter than about $6 \times 10^{-17} \text{ erg s}^{-1} \text{ cm}^{-2}$ lie systematically above the best-fit double power-law. The emergence of a population of normal star-forming galaxies at faint fluxes can explain this excess. This is demonstrated in Figure 7 plotting the expected star-forming galaxy number counts, estimated by integrating the X-ray luminosity func-

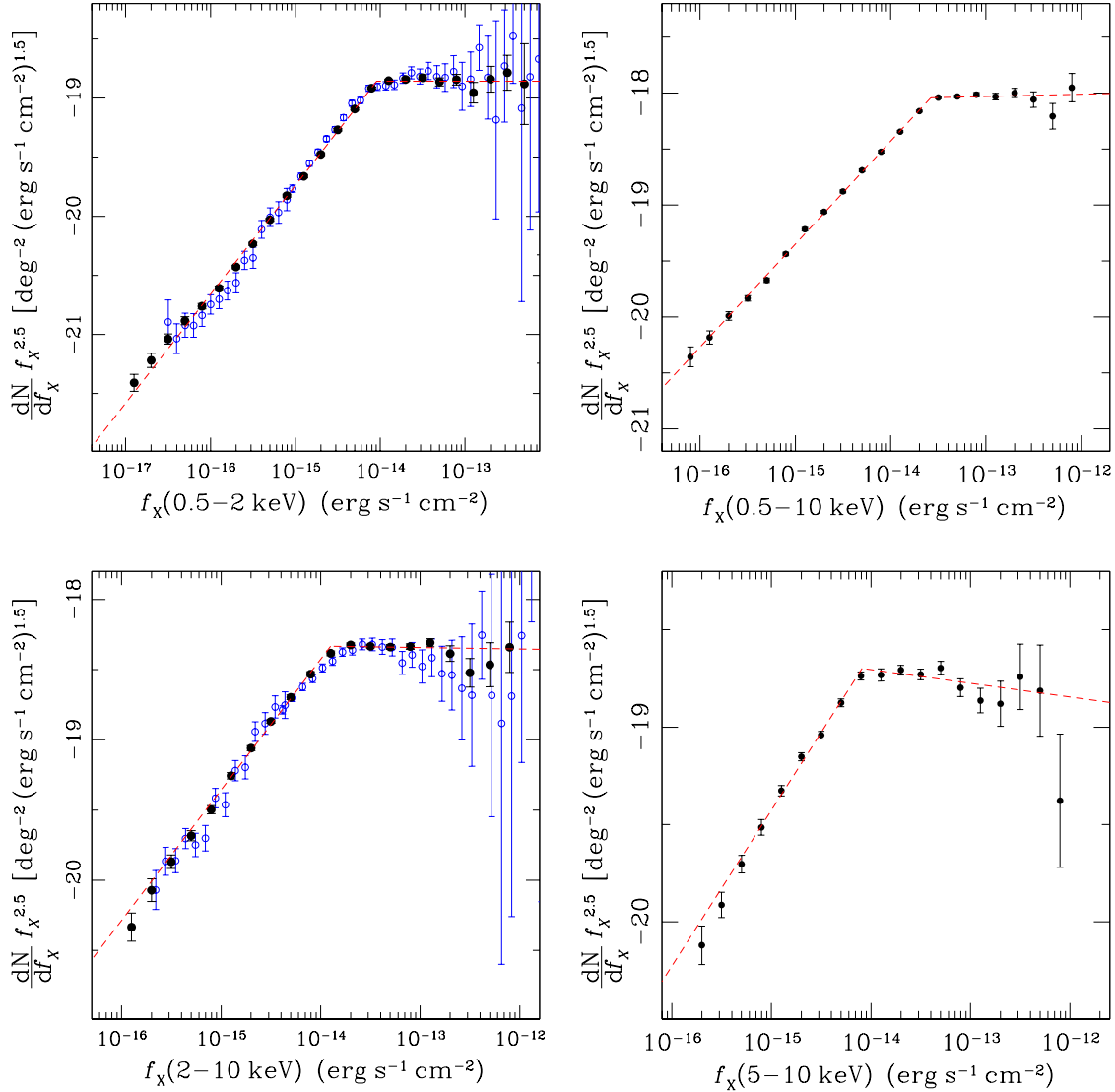


Figure 5. In all panels the (black) filled circles are the differential number counts normalised to the Euclidean slope in the soft, total, hard and ultra-hard bands for the combined *Chandra* surveys listed in Table 1. The error-bars are estimated using bootstrap resampling as discussed in the text. The (red) dashed line in each panel is the maximum likelihood fit to the data. The (blue) open circles in the soft and the hard band count panels are the differential number counts from the ChaMP survey and the Chandra Deep Fields estimated by Kim et al. (2007a). For the ultra-hard band there is no systematic study of the dN/dS to compare with.

Table 2. X-ray number count best-fit parameters for the differential counts adopting the double power of equation 1. The cumulative counts $N(> f_x)$ are obtained using equation 2

Band (1)	Sources (2)	β_1 (3)	β_2 (4)	$\log f_b$ (5)	K (6)
Soft	4756	$-1.58^{+0.02}_{-0.03}$	$-2.50^{+0.07}_{-0.05}$	$-0.04^{+0.06}_{-0.05}$	1.51 ± 0.03
Hard	2565	$-1.56^{+0.04}_{-0.04}$	$-2.52^{+0.07}_{-0.09}$	$+0.09^{+0.08}_{-0.05}$	3.79 ± 0.08
Ultra-Hard	1081	$-1.70^{+0.08}_{-0.06}$	$-2.57^{+0.07}_{-0.09}$	$-0.09^{+0.06}_{-0.10}$	2.36 ± 0.08
Total	5561	$-1.58^{+0.01}_{-0.02}$	$-2.48^{+0.06}_{-0.03}$	$+0.42^{+0.07}_{-0.05}$	3.74 ± 0.05

The columns are: (1): Spectral band; (2): Number of sources above the 4×10^{-6} detection threshold in a given energy band; (3) faint end index of the double power-law; (4): bright end index of the double power law; (5): log of the break flux in units of $10^{-14} \text{ erg cm}^{-2} \text{ s}^{-1}$. (6): Normalisation in units $10^{16} \text{ deg}^{-2} / (\text{erg cm}^{-2} \text{ s}^{-1})$.

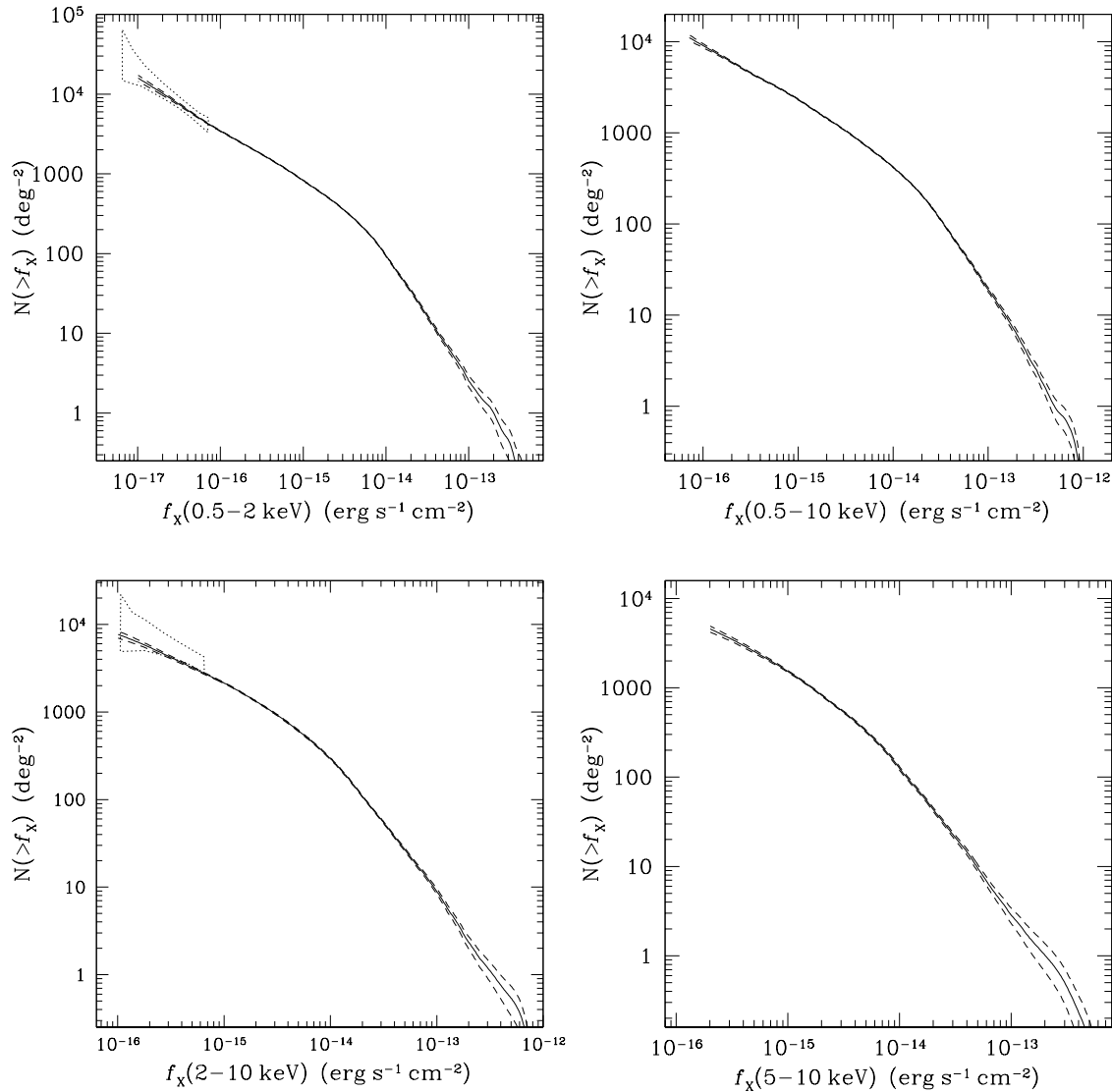


Figure 6. Cumulative number counts in the soft, total, hard and ultra-hard bands for the combined *Chandra* surveys listed in Table 1. The continuous black line is the estimated number counts, the dashed lines correspond to the 1σ rms uncertainty estimated using bootstrap resampling of the data. For clarity the maximum likelihood fits to the data are not shown. The 1 Ms CDF-N fluctuation analysis results for the soft and hard bands (Miyaji & Griffiths 2002) are shown with the dotted line wedges.

tion of these systems at low redshift (Georgakakis et al. 2006) assuming pure luminosity evolution of the form $\propto (1+z)^{2.4}$ (e.g. Georgakakis et al. 2007).

Contrary to the soft-band, the 2-10 and 5-10 keV counts at faint fluxes in Figure 5 show tentative evidence, significant at $\approx 2\sigma$ level, for a flattening of the faint-end slope at the limit of the deepest X-ray survey of the sample, the CDF-North. Kim et al. (2007a) have shown that the $\log N - \log S$ distribution of sources depends on their hardness ratio, HR. Sources with $HR > 0$ have steep differential counts that do not show evidence for a break in the slope at the flux limit of the ChaMP survey. In contrast, sources with $HR < 0$, show the characteristic break in their number count distribution. It is suggested that sources with $HR > 0$ lie, on average, at redshifts lower than the population with $HR < 0$ and as a result they do not show the cosmological evolutionary effects that cause the break in the $\log N - \log S$ (Harrison et al. 2003; Kim et

al. 2007a). The change in slope at the faint-end of the 2-10 and 5-10 keV counts is likely related to the relative contribution of sources with $HR \leq 0$.

Figure 8 plots the contribution of the point sources to the diffuse X-ray background (XRB) in different spectral bands. This is estimated by integrating the double power-law relation using the best-fit parameters listed in Table 2. For the level of XRB we adopt the average flux densities of $(7.52 \pm 0.35) \times 10^{-12} \text{ erg s}^{-1} \text{ cm}^{-2} \text{ deg}^{-2}$ for the 0.5-2 keV band from Moretti et al. (2003) and $(2.24 \pm 0.11) \times 10^{-11} \text{ erg s}^{-1} \text{ cm}^{-2} \text{ deg}^{-2}$ for the 2-10 keV range from De Luca & Molendi (2004). For the total spectral band, 0.5-10 keV, we add the values above and estimate an XRB flux density of $(2.99 \pm 0.12) \times 10^{-11} \text{ erg s}^{-1} \text{ cm}^{-2} \text{ deg}^{-2}$. In the case of the 5-10 keV band we assume $\Gamma = 1.41$ and the 2-10 keV XRB flux density determined by De Luca & Molendi (2004) to estimate $(1.23 \pm 0.06) \times 10^{-11} \text{ erg s}^{-1} \text{ cm}^{-2} \text{ deg}^{-2}$. The fraction

Table 3. Resolved X-ray Background fractions

Band (1)	limit (2)	fraction (3)
Soft	1×10^{-17}	82 ± 4
Hard	1×10^{-16}	74 ± 4
Ultra-Hard	2×10^{-16}	72 ± 4
Full	7×10^{-17}	81 ± 3

The columns are: (1): X-ray energy band; (2): flux limit in the corresponding spectral band that the resolved XRB fraction is estimated. The units are $\text{erg s}^{-1} \text{cm}^{-2}$. At these flux limits the area curve of the deepest survey in the sample, the CDF-N, drops to about 1 per cent of its maximum value; (3) Per cent fraction of the XRB resolved into point sources.

of the XRB resolved in point sources in different energy bands to the limits of the deepest survey in the sample are listed in Table 3. In addition to the statistical uncertainty listed in that table there is a systematic error of about 10-20 per cent related to the uncertainty in the determination of the absolute normalisation of the XRB (e.g. Revnivtsev et al. 2003, 2005). In Table 3 the 2-10 and 5-10 keV bands resolve similar fractions of the XRB, 74 ± 4 and 72 ± 4 per cent respectively. This is consistent with the work of Worsley et al. (2005). In that study the fraction of the XRB resolved into point sources is nearly constant at 2–6 keV and drops substantially at energies > 6 keV to about 50 per cent in the 8–12 keV band.

The resolved XRB fractions in the 2-10 and 5-10 keV bands can be used to place constraints on the spectral shape of the unresolved XRB. First, the difference in the sensitivity in the two energy bands needs to be accounted for by matching their flux limits. The 5-10 keV flux limit of $2 \times 10^{-16} \text{ erg s}^{-1} \text{cm}^{-2}$ corresponds to $f_X(2-10) = 3.6 \times 10^{-16} \text{ erg s}^{-1} \text{cm}^{-2}$ for $\Gamma = 1.4$, i.e. the mean spectrum of the XRB. At this flux 70 \pm 4 per cent of the XRB in the 2-10 keV band is resolved into point sources. We then assume that there is a single population that is responsible for the unresolved part of the XRB in both the 2–10 (30 \pm 4 per cent) and 5–10 keV (28 \pm 4 per cent) bands. There has been speculation recently on whether the unresolved background at hard energies is produced by Compton thick AGN (Worsley et al. 2005; Gilli et al. 2007). In order to test this possibility we adopt for the X-ray spectral shape of this population the Compton reflection models of Magdziarz & Zdziarski (1995) as implemented in the PEXRAV spectral energy distribution of XSPEC. We assume a mean redshift $z \approx 1$, a solid angle of 2π , solar abundance for all elements and an average inclination relative to the line of sight $\cos i = 0.45$. Only the reflection component was used, i.e. no direct radiation. We find that if the entire 30 per cent of the unresolved background in the 2-10 keV band (to the limit $f_X(2-10) = 3.6 \times 10^{-16} \text{ erg s}^{-1} \text{cm}^{-2}$) is produced by such sources, then their contribution to 5-10 keV XRB is 39 per cent, which exceeds the unresolved fraction (28 \pm 4 per cent) at the 2.8σ level. Moving the mean redshift of the Compton thick AGN population to $z \approx 2$ reduces the significance of the excess to 2.2σ . We conclude that either some of the sources in the 5-10 keV selected sample lie below the flux limit $f_X(2-10) = 3.6 \times 10^{-16} \text{ erg s}^{-1} \text{cm}^{-2}$ or the unresolved XRB fraction in the 2-10 keV band cannot be entirely due to a single population of Compton thick AGN.

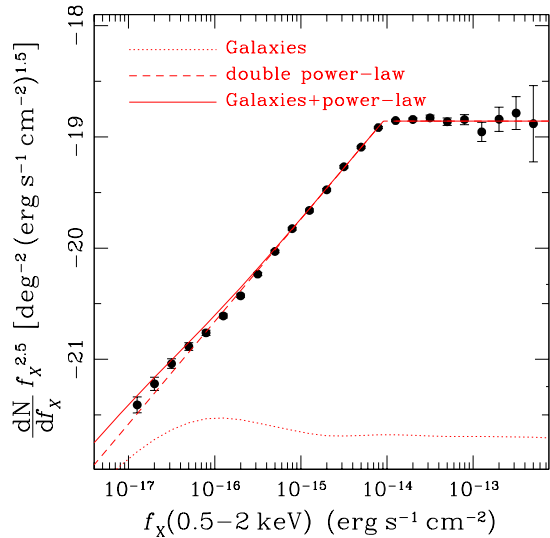


Figure 7. Soft-band differential source counts in comparison with the dN/df_X for star-forming galaxies (Georgakakis et al. 2007). The surface density of these sources can account for the excess counts above the broken double power-law expectation at fluxes below about $6 \times 10^{-17} \text{ erg s}^{-1} \text{cm}^{-2}$.

7 CONCLUSIONS

A new method is presented for determining the sensitivity of X-ray imaging observations, which accurately estimates the probability of detecting a source with a given X-ray flux accounting for observational effects, such as vignetting, flux estimation biases and the fraction of spurious sources expected in any source catalogue. A major advantage of the proposed method is that it is analytical and therefore does not require a large number of cumbersome ray tracing simulations to quantify the effects above. We demonstrate how to use the sensitivity maps determined by our new method in order to accurately estimate the number counts in different X-ray spectral bands, using all the detected sources, even those with few counts, for which the completeness and flux bias corrections are large. This method is applied to real *Chandra* data. The sample includes both deep pencil-beam and shallow wide-area surveys covering a total area of about 11.8 deg^2 and includes over 6000 unique sources. We present, for the first time, the X-ray counts in the 5-10 keV band over a wide range of X-ray fluxes (4 dex) and determine the break flux in this band. We also find evidence for an upturn in the 0.5-2 keV differential counts below about $6 \times 10^{-17} \text{ erg s}^{-1} \text{cm}^{-2}$, which we attribute to the emergence of a population of star-forming galaxies at faint fluxes. Based on the fraction of the XRB resolved in the 2-10 and 5-10 keV bands we argue that a single population of Compton thick AGN cannot by itself produce the entire unresolved X-ray background in the 2-10 keV energy range.

8 ACKNOWLEDGEMENTS

We thank the anonymous referee for providing constructive comments and suggestions that improved this paper. This work has been supported by funding from the Marie-Curie Fellowship grant MEIF-CT-2005-025108 (AG) and the STFC (ESL). The

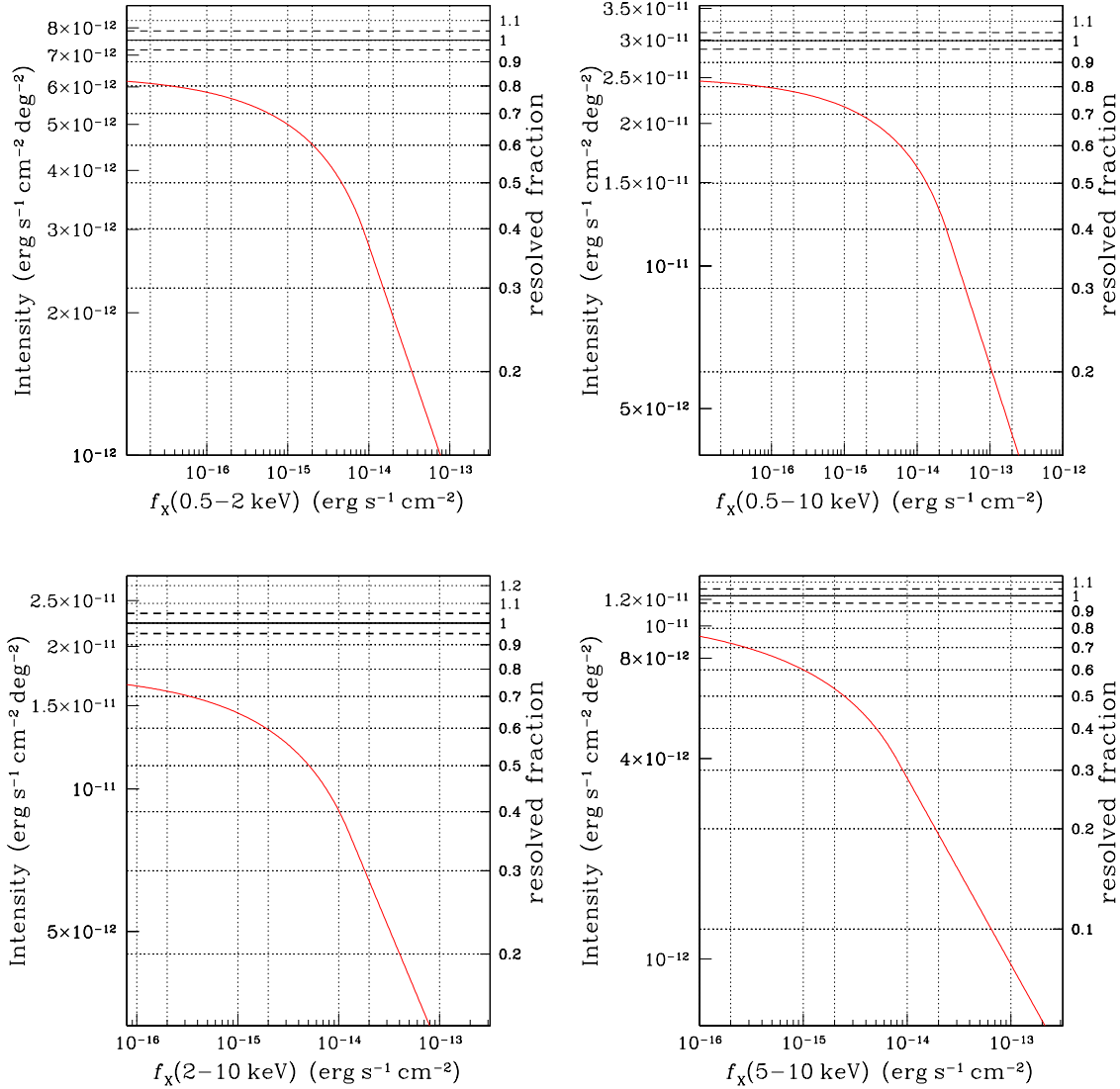


Figure 8. Integrated intensity and contribution to the diffuse X-ray background of the point sources detected in different spectral bands. The (red) curves are estimated from the maximum likelihood fits to the differential number counts. The level of the X-ray background is shown with the horizontal continuous line. The dashed lines correspond to the statistical 1σ rms uncertainty to this value.

data products used in this paper are available for download at <http://astro.ic.ac.uk/research/xray/chandrasurveys.shtml>

REFERENCES

- Akylas A., Georgantopoulos I. & Georgakakis A., Kitsionas S., Hatziminaoglou E., 2006, *A&A*, 459, 693
- Aird J., Nandra K., Georgakakis A., Laird E. S., Steidel C. C., Sharon C., 2008, *MNRAS*, submitted
- Basilakos S., Plionis M., Georgakakis A., Georgantopoulos I., 2005, *MNRAS*, 356, 183
- Basilakos S., Georgakakis A., Plionis M., Georgantopoulos I., 2004, *ApJ*, 607L, 79
- Cappelluti N., et al., 2007, *ApJS*, 172, 341
- De Luca A. & Molendi S. 2004, *A&A*, 419, 837
- Georgakakis A. E., Chavushyan V., Plionis M., Georgantopoulos I., Koulouridis E., Leonidaki I., Mercado A., 2006, *MNRAS*, 367, 1017
- Georgakakis A., Rowan-Robinson M., Babbedge T. S. R., Georgantopoulos I., 2007, *MNRAS*, 377, 203
- Gilli R., Comastri A., Hasinger G., 2007, *A&A*, 463, 79G
- Gilli R., et al., 2005, *A&A*, 430, 811
- Harrison F. A., Eckart M. E., Mao P. H., Helfand D. J., Stern D., 2003, *ApJ*, 596, 944
- Hasinger G., Miyaji T., Schmidt M., 2005, *A&A*, 441, 417
- Kenter A. T. & Murray S. S., 2003, *ApJ*, 584, 1016
- Kim. M., et al., 2007a, *ApJ*, 659, 29
- Kim. M., et al., 2007b, *ApJS*, 169, 401
- La Franca F., et al., 2005, *ApJ*, 635, 864
- Magdziarz & Zdziarski, 1995, *MNRAS*, 273, 837
- Miyaji T., et al., 2007, *ApJS*, 172, 396
- Moretti A., Campana S., Lazzati D., & Tagliaferri G. 2003, *ApJ*, 588, 696
- Nandra K., Laird E. S., Steidel C. C., 2005a, *MNRAS*, 360L, 39
- Nandra K., Laird E. S., Adelberger K., Gardner J. P., Mushotzky R. F., Rhodes J., Steidel C. C., Teplitz H. I., Arnaud K. A., 2005b, *MNRAS*, 356, 568

Revnitsev M., Gilfanov M., Jahoda K., Sunyaev R., 2005, *A&A*, 444, 381

Revnitsev M., Gilfanov M., Sunyaev R., Jahoda K., Markwardt C., 2003,
A&A, 411, 329

Wang Q. D., 2004, *ApJ*, 612, 159

Worsley M. A. et al., 2005, *MNRAS*, 357, 1281